Surfaces and Interfaces 80 (2026) 108215

Contents lists available at ScienceDirect

Surfaces and Interfaces

journal homepage: www.sciencedirect.com/journal/surfaces-and-interfaces

Tuning anodizing conditions in tartaric acid containing bath for strengthening fiber metal laminates with peek/carbon in composite for aerospace applications

R. Miranda, A. Zaffora *, V. Fiore, F. Di Franco, M. Santamaria, A. Valenza

Department of Engineering, University of Palermo, Viale delle Scienze, 90128 Palermo, Italy

ARTICLE INFO

Keywords:
Fiber metal laminates (FMLs)
Tartaric-sulfuric acid (TSA) anodizing
Corrosion resistance
Polyether ether ketone (PEEK) composites
Aerospace materials

ABSTRACT

The article investigates the enhancement of Fiber Metal Laminates (FMLs) in aerospace applications by exploring the effects of Tartaric-Sulfuric Acid (TSA) anodizing and its modifications on 2024-T3 and 7075-T6 aluminium alloys. The research aims to optimize the anodized aluminium's surface morphology to improve both corrosion resistance and mechanical properties, in the context of adhesive bonding with carbon-reinforced Polyether Ether Ketone (PEEK) composites. To understand how treatment parameters like tartaric acid concentration, temperature, and anodizing time affect oxide layer formation on aluminium, these variables were systematically varied. The results show that the modification on TSA anodizing processes parameters, effectively enhances the mechanical performance and corrosion resistance of FMLs by tailoring the morphology of the oxide layer. The anodized FML samples demonstrated superior mechanical properties and corrosion resistance compared to mechanically treated samples, making these anodizing techniques particularly promising for aerospace applications requiring durable and lightweight materials.

1. Introduction

The demand for lightweight yet structurally robust materials has encouraged the research to overcome the classic approach used today in industrial sectors such as aerospace, automotive and naval. Monolithic structures are not compatible with lightweight construction due to their inherent nature, while using the right material in the best place generates the right combination of mechanical performance and lightness. Today, the tailoring of the structures is a key role in the design process and the focus of a good project is the detailed study of the joint between the different materials used [1–3]. In this context, adhesive bonding plays a critical role facilitating weight reduction and enhanced structural integrity [4–8]. However, the performance of adhesive joints is heavily influenced by surface properties, particularly in the context of challenging aerospace environments characterized by extreme temperatures, corrosive atmospheres, and mechanical stresses. In the pursuit of enhancing the performance of adhesive bonding in aerospace applications, the role of surface modification techniques has become increasingly paramount. Among these techniques, anodizing stands out as a versatile and effective method for tailoring surface properties to optimize adhesive bond strength and durability. Anodizing offers a unique solution to this dual challenge: the formation of an oxide layer that has both an external porous part, useful in interlocking with adhesives, and an underlying barrier part that protects the substrate from corrosion [9–11]. Furthermore, the microstructure and morphology of the anodized surface can be precisely engineered to promote mechanical interlocking between the adhesive and substrate, increasing bond strength and resistance to peel and shear forces [12–15]. The duality of corrosion resistance and mechanical properties holds particular significance in the context of adhesive bonding [16,17]. The integrity of adhesive bonds hinges on the ability of the substrate surface to withstand degradation while maintaining robust mechanical interlocking with the adhesive. For example, Chen et al. [18] evaluated oxalic and phosphoric acid as anodizing bath to enhance the mechanical performance of adhesive joint between aluminium alloy 5754 to glass-fiber reinforced polypropylene random copolymer. They concluded that phosphoric acid anodizing significantly improves the bonding properties of aluminium alloy/polymeric composite hybrid joints. This is due to the formation of needle-shaped, honeycomb-like microstructures, which enhance mechanical interlocking and chemical bonding. The resulting higher tensile shear strength, surface roughness, and surface energy lead to superior adhesion, made this technique promising for automotive applications

* Corresponding author.
E-mail address: andrea.zaffora@unipa.it (A. Zaffora).

https://doi.org/10.1016/j.surfin.2025.108215
Received 12 May 2025; Received in revised form 27 November 2025; Accepted 1 December 2025
Available online 2 December 2025

requiring durable, high-performance hybrid joints.

Historically, the predominant solution bath utilized in the aerospace industry for the anodizing process involved chromic acid (CAA). However, the utilization of this reagent has been prohibited due to the significant risk of chromium (VI) pollution, which is a carcinogenic agent [19]. Although CAA was renowned for generating a porous layer that facilitated robust mechanical interlocking and corrosion protection, the imperative now is to identify alternative and more sustainable methodologies. One potential substitute for CAA is anodizing employing tartaric-sulfuric acid (TSA), which yields a layer characterized by improved corrosion resistance. Nonetheless, a drawback arises from the exceedingly small pores formed, hindering effective interlocking with the polymeric resin, used as matrix of the composite substrate. For this reason, other anodizing baths have been considered. In particular, the current approach to address the limitations of the CAA solution is to split the problem. This means that when improved interlocking in adhesive joints or painting is required, phosphoric acid anodizing techniques are used to generate larger pores, but at the cost of reduced corrosion resistance. Conversely, when more corrosion protection is needed, techniques that produce smaller diameter pores are employed [20]

When considering the integration of different materials through bonding, the merging of metals with polymer composites emerges as a versatile solution that effectively addresses the dual need for lightweight design and robust mechanical performance [21–24].

The relentless pursuit of lightweight yet resilient materials has propelled fiber reinforced plastics (FRPs) to the forefront of innovation. These advanced materials, comprising a matrix reinforced with high-strength fibers, offer an attractive blend of low density, exceptional mechanical properties, and tailored performance characteristics. For example, with the evolution of aerospace structures towards increasingly lightweight designs, FRPs have emerged as indispensable building blocks, revolutionising the bonding landscape.

In the 1970s, a specialized category of lightweight hybrid materials known as fiber metal laminates (FMLs) was developed to address the complex demands of aerospace engineering. These laminates comprise alternating thin layers of aluminium alloy and fiber-reinforced composite (FRC), offering a unique amalgamation of properties. By combining the high strength, stiffness, and excellent fatigue resistance of composites with the machinability, formability, and toughness of metals, FMLs represent a compelling solution for aerospace applications.

Commercially available FMLs typically feature aluminium alloy foils such as 2024-T3 or 7075-T6, reinforced with polymer composites containing glass, carbon, or aramid fibers, known as GLARE, CARALL, or ARALL, respectively [25–29]. However, mentioned composites are made with thermosetting resin, which has better fiber wettability and different adhesion techniques, given that these resins are liquid before the polymerization process.

With growing emphasis on environmental sustainability, there is an increasing interest in FMLs reinforced with carbon fibers and utilizing thermoplastic matrices. Thermoplastics offer advantages over thermosets, including recyclability, and enhanced impact and fatigue resistance. Consequently, there is a push within the aerospace industry towards the adoption of thermoplastics as matrix materials for composite layers [30–34].

Among thermoplastic polymers, techno-polymers stand out for their superior strength and elastic modulus, particularly at high temperatures. Polyether ether ketone (PEEK), a semi-crystalline polymer, exemplifies this, displaying glass transition temperature (T_g) and melting point of 143 °C and 343 °C, respectively [35,36]. With an elastic modulus ranging from 2 to 4 GPa and tensile strength up to 120 MPa, PEEK offers remarkable mechanical properties suitable for aerospace and biomedical applications [37–40]. Jiang et al. [41] explored enhancing the interfacial bonding between titanium and PEEK through cerium surface treatment coupled with sandblasted metal sheets. Cerium surface modification enhanced titanium sheet wettability, facilitating spontaneous spreading and tight adhesion of PEEK melt on the sandblasted titanium treated with cerium and dried at 80 °C (S-RE-Ti) surfaces. The resulting CF/PEEK (S-RE-Ti) exhibited significantly improved flexural strength and interlaminar shear strength with increments of 180 % and 40 %, respectively, compared to the fiber metal laminates made using reference metal, the sandblasted titanium (S-Ti). The interface's single lap shear strength was boosted by 178 % compared to S–Ti. Cohesive failure at the titanium-PEEK interface indicated effective chemical bonding due to cerium elements. They demonstrated that cerium surface modification method held promise for improving FML interfacial bonding, offering a straightforward and effective approach for chemically bonding metal-resin interfaces.

This research aims to contribute to increase the knowledge of the potential uses of TSA modification for dual-purpose in adhesive bonding, i.e., corrosion resistance and the mechanical performance. To the author's knowledge, no such applications are found in the literature, and they are being applied here for the first time. Previous study has reported a two-step anodizing procedure for AA7075-T6, combining TSA and phosphoric–sulfuric acid (PSA) electrolytes, which resulted in improved interfacial interlocking with thermoplastic polymers and enhanced corrosion resistance [42]. The novelty of the present work lies in developing a one-step TSA process, specifically tailored for both aerospace-grade AA2024-T3 and AA7075-T6 alloys, to simultaneously enhance the performance of carbon/PEEK-based thermoplastic FMLs and enable implementation in existing industrial anodizing lines without introducing additional steps or equipment. The effects of varying the concentration of tartaric acid in the anodizing bath and the anodizing parameters (time, temperature, and potential) on the morphological features of the porous oxide layer (such as pore diameter, thickness of porous layer and thickness of barrier layer) were evaluated, as well as their impact on the corrosion and mechanical strength of the FMLs.

2. Experimental

2.1. Materials

Aluminium alloys 7075-T6 and 2024-T3, obtained from Good-Fellow® Cambridge Ltd. (United Kingdom), were chosen as the metallic substrates, with a nominal thickness of 0.6 mm and 1 mm, respectively. Composition and mechanical properties of as-received samples are reported in Table 1. The composite substrate comprised two or three layers of carbon fabric reinforcement and three or four layers of 0.2 mm thick polyether ether ketone (PEEK Ketaspire® from Solvay) as the matrix (the amount depended on the aluminium alloy employed as exposed in subsequent paragraphs). The carbon fabric reinforcement, featuring a 3k plain weave architecture and an areal weight of 200 g/m^2, was supplied by Hexcel (utilizing HexTow® AS4 fibers).

Table 1
Mechanical properties and chemical composition of as-received aluminium alloys.

Alloys	Young modulus [GPa]	Tensile strength [MPa]	Elongation at break [%]		Shear strength [MPa]	
2024-T3	73.1	483	18		283	
7075-T6	71.7	572	11		331	
	Al	**Zn**	**Mg**	**Mn**	**Cu**	**Si**
2024-T3	90.7–94.7 %	≤0.25 %	1.2–1.8 %	0.3–0.9 %	3.8–4.9 %	≤0.5 %
7075-T6	87.1–91.4 %	5.1–6.1 %	2.1–2.9 %	≤0.3 %	1.2–2 %	≤0.4 %

Table 2
Details of the anodizing conditions for TSA processes on aluminium alloys.

Codes	Tartaric acid concentration [g/l]	Sulphuric acid concentration [g/l]	Potential [V]	Temperature [°C]	Time [min]
TSA 20	80	40	20	37	10
T+SA 20	150	40	20	37	10
TSA 14	80	40	14	55	10
T+SA 14	150	40	14	55	10
TSA ML	80	40	14	37	20
T+SA ML	150	40	14	37	20

2.2. Aluminium alloy surface treatments

Before carrying out the anodizing processes, the metal alloys were suitably prepared to create an optimal substrate. The 2024-T3 and 7075-T6 aluminium specimens were first mechanically polished with different abrasive papers, starting with a #500 grit, then a #800 grit, and finishing with a #1200 grit. Afterwards, the specimens were first cleaned in an ultrasonic acetone bath for 5 min and then rinsed with deionised water. Subsequently, the specimens were immersed in a 10 wt % solution of sodium hydroxide (NaOH) at a temperature of 60 °C for 30 s to carry out etching, that is, the removal of the oxide layer that naturally forms on the aluminium surface. After rinsing in deionised water, they were immersed in a 30 %v/v solution of nitric acid (HNO_3) at room temperature for 15 s to carry out desmutting process, which aims to remove residues from the previous treatment and to even out the surface finish. Finally, the specimens were rinsed in deionised water and dried in oven at 80 °C for 24 h.

Anodizing process was employed as surface modification electrochemical treatment on the aluminium alloys. Tartaric-sulfuric acid (TSA) was used as reference bath and compared with modified solutions, summarized in Table 2, varying the concentration of tartaric acid, temperature, time, and applied potential.

The identifying codes refer to the standard bath concentrations of the TSA [43] and T+SA (i.e. TSA with a higher amount of tartaric acid) studied by Martinez-Viademonte et al. [44]. In both TSA and T+SA, the number 20 refers to a potential of 20 V, a temperature of 37 °C, and an anodizing time of 10 min, while the number 14 corresponds to a potential of 14 V, a temperature of 55 °C and an anodizing time of 10 min. The letter ML refers to a procedure with mixed and longer parameters, in fact it uses a potential of 14 V but with a temperature of 37 °C and an anodizing time doubled to 20 min. For all the conditions investigated, the concentration of sulphuric acid was kept constant (i.e., 40 g/l). In addition to the time indicated in the table, each anodizing process includes a linear potential ramp from zero to the steady state value, lasting one minute.

Mechanical treatment on the surfaces of both aluminium alloys was employed as reference treatment for the FMLs. This treatment was carried out with an orbital sander equipped with #80 grit abrasive paper and was denominated with MT identifying code (i.e., Mechanically Treated).

2.3. Surface morphology analysis

Surface morphology assessment in the initial phase involved scanning electron microscope (SEM) imaging. This analysis was crucial in the decision of which anodizing parameters could create in determining the optimal anodizing parameters for creating a suitable oxide layer with appropriately sized nanopores for adhesive joints. The morphology of the porous layer obtained through anodizing was examined using a FEI Quanta 200 FEG scanning electron microscope.

The mean pore diameter and its standard deviation were determined for each electrochemically treated surface by analysing 50 measurements using the commercial software ImageJ.

2.4. Corrosion resistance measurements

Open circuit potential (OCP) and electrochemical impedance spectroscopy (EIS) were performed to study the corrosion resistance of the metallic specimens. This characterization was employed to evaluate the corrosion resistance of the samples. For these measurements, a Parstat 4000 potentiostat was employed. Throughout the experiments, the specimens underwent immersion in an aqueous solution comprising 3.5 wt % NaCl, mimicking seawater conditions. Open circuit potential (OCP) measurement utilized the Ag/AgCl reference electrode (0.197 V vs. SHE), submerged in the solution for a duration of 30 min. Following this, impedance measurement was conducted with a platinum mesh counter electrode under ambient pressure and temperature conditions. a.c. potential signal amplitude was 10 mV and its frequency ranged between 0.1 Hz and 100 kHz. Finally, a polarisation curve was recorded in the same seawater-mimicking solution, from −200 mV relative to the OCP to 1 V Ag/AgCl, to evaluate the impact of the different anodizing conditions on corrosion potential, pitting potential and passivity current density. Reported polarization curves are the average of three measurements carried out to ensure repeatability.

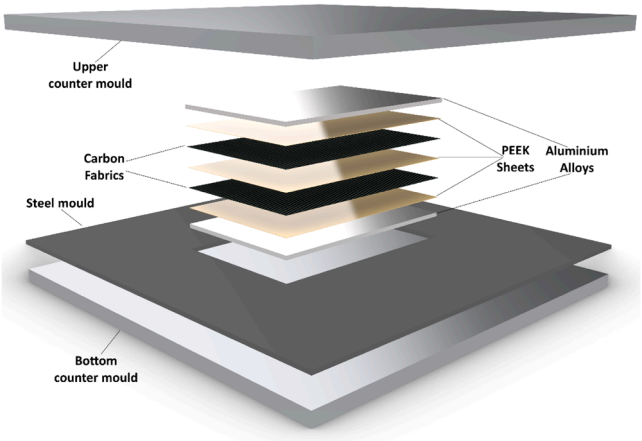

Fig. 1. Schematization of stacking sequence of compression moulding in hot press for 7075 and 2024 FMLs.

2.5. Fabrication of the FMLs

Compression moulding using a CARVER Autofour/3012-PLH hot press was chosen as the manufacturing process for producing the FMLs. Samples were fabricated through a layering process, alternating PEEK foil and carbon fabrics at the top the aluminium sheet as visible in Fig. 1. The temperature-pressure cycle was applied as follows: once the temperature reached 385 °C, specimens of 150 mm x 100 mm, with the thickness depending on the metal substrates, were held at this temperature for 20 min at a pressure of 41 bar. Before reaching the maximum temperature, the pressure was increased gradually. Cooling was conducted in the hot press with a controlled air/water circuit while maintaining the same pressure. Each component of the fiber metal laminates before of the compression process was dried in oven at 80 °C for 24 h.

The 0.2 mm thick PEEK sheets were previously manufactured by compression moulding using the same thermoforming press, pre-heated at 385 °C. In particular, 4.5 g of PEEK in pellet form were placed inside a steel mould and counter mould and a pressure of 41 bar was applied for 20 min. For 2024-T3 aluminium alloy (1 mm nominal thickness), 4 PEEK sheets alternating with 3 layers of carbon fabric were stacked, resulting in an FML with a thickness of approximately 3 mm. For 7075-T6 aluminium alloy (0.6 mm nominal thickness), 3 sheets of PEEK alternating with 2 layers of carbon fiber were used, obtaining an FML with approximately 1.6 mm thickness. The different number of PEEK layers is due to the requirement of creating a composite layer of equal thickness with the aluminum layers. Mechanical behavior of metals may differ after the technological process with respect to that of as-received samples. However, all samples were subjected to the same thermal cycle, therefore the comparisons in the results after the treatments remain valid, even if the properties of the metals could be changed.

Afterward, the FMLs were cut by using a rotary blade (Bosh GCM 800 SJ) to obtain samples suitable for mechanical testing.

2.6. Mechanical performance evaluation

The interlaminar shear strength (ILSS) of FMLs was determined through short beam shear tests (SBS). For each surface treatment, five replicates were tested according to ISO 14,130 guidelines [45], utilizing a WANCE model ETM-C universal testing machine (UTM) equipped with a 50 kN load cell. The span distance was set at 10 mm while the crosshead speed was fixed at 1 mm/min. The specimens were geometrically shaped at 20 × 10 mm with the thickness depending on the resulting FMLs. The ILSS was evaluated according to the following Eq. (1):

$$\tau = \frac{3F}{4bh} \tag{1}$$

Where F is the failure load, b and h are the width and the total thickness of the samples, respectively.

The three-point bending tests were carried out using the same UTM, used for SBS tests, according to ASTM D790 standard [46]. The thickness-to-span ratio was chosen to be 1:32, so for the FML made from 2024-T3 with a thickness of 3 mm and a length of 110 mm, a span of 96 mm was used. Similarly, for the FML made from 7075-T6 with a thickness of 1.8 mm and a length of 70 mm, a span of 57 mm was used. In accordance with the standard, the crosshead displacement was set at 5 mm/min and 3 mm/min for 2024-T3 for 7075-T6, respectively.

The flexural stress, modulus of elasticity and percentage deformation were calculated as follows:

$$\sigma = \frac{3PL}{2bd^2} \tag{2}$$

$$E = \frac{L^3 m}{4bd^3} \tag{3}$$

$$\boldsymbol{\varepsilon} = 100 \cdot \frac{6Dd}{L^2} \tag{4}$$

Where P is the applied load and D is the maximum deflection measured at the centre of the specimen under that load. L, d, b are the support span, specimens thickness and width, respectively. The modulus of elasticity was calculated using m, i.e., the slope of the tangent to the initial straight-line portion of the load-deflection curve, N/mm of deflection.

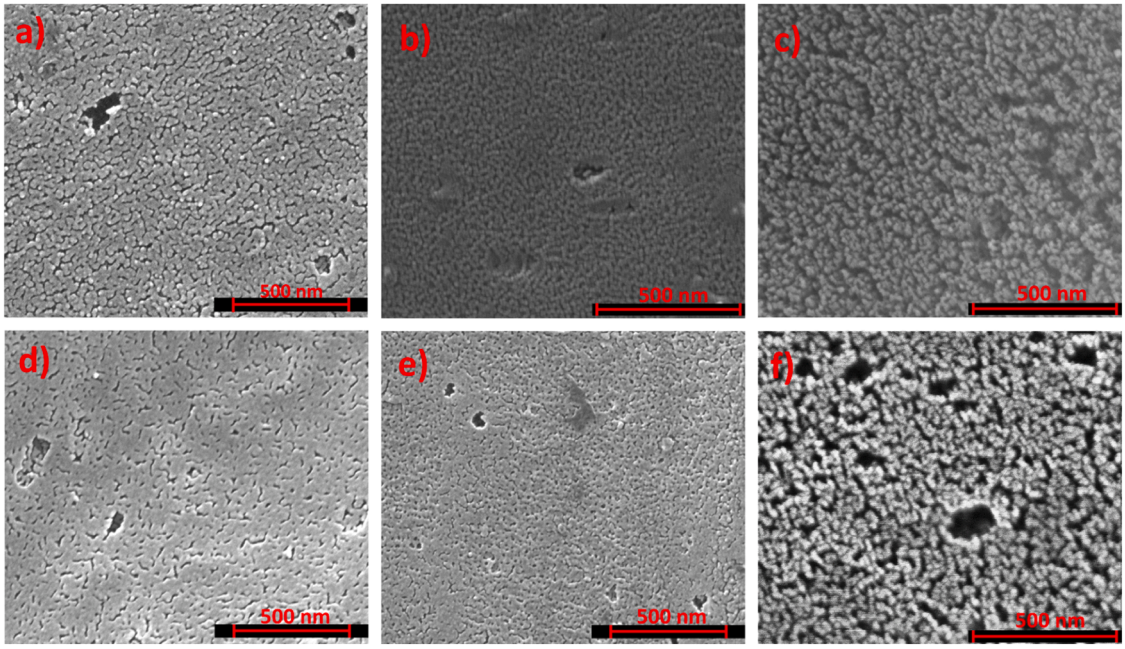

Fig. 2. SEM micrographs of surfaces of anodized 2024-T3 aluminium alloy: a) TSA ML, b) TSA 20, c) TSA 14, d) T+SA ML, e) T+SA 20, and f) T+SA 14 samples.

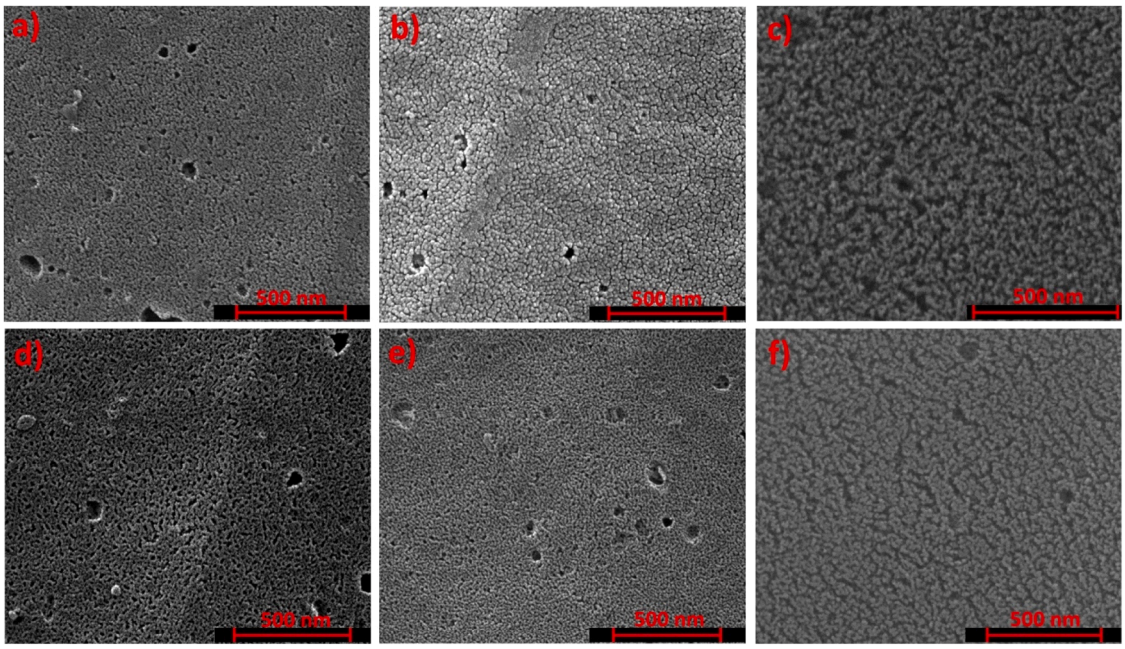

Fig. 3. SEM micrographs of surfaces of anodized 7075-T6 aluminium alloy: a) TSA ML, b) TSA 20, c) TSA 14, d) T+SA ML, e) T+SA 20, and f) T+SA 14 samples.

Table 3
Average pores diameters and their standard deviation varying the surface treatments.

	TSA ML [nm]	TSA 20 [nm]	TSA 14 [nm]	T+SA ML [nm]	T+SA 20 [nm]	T+SA 14 [nm]
2024-T3	9.5 ± 2.8	11.3 ± 2.6	16.8 ± 4.6	8.8 ± 2	7.0 ± 2.2	10.4 ± 2.4
7075-T6	10.7 ± 1.7	8.3 ± 2.2	15.4 ± 3.4	15.5 ± 3.8	11.5 ± 2.6	17.9 ± 4.2

3. Results and discussions

3.1. Preliminary analyses of aluminium alloy substrates

3.1.1. Morphology of the porous oxide layers

Fig. 2 and Fig. 3 show the SEM micrographs of the surfaces of all the investigated metal samples, (2024-T3 and 7075-T6), anodized in different process conditions (i.e. tartaric acid concentrations, bath temperature, final voltage and anodizing times, as described in Table 2).

Regarding aluminium alloy 2024, increasing tartaric acid concentration in anodizing bath resulted in a reduced porosity of the surface oxide layer (i.e., T+SA 20 in Fig. 2e generated a porous layer barely visible also at high magnification), when anodizing process was carried out at 37 °C (see Fig. 2b-e), consistent with previous findings [44], whilst it resulted in a change of porous layer morphology when the sample was anodized at 55 °C (see Fig. 2c-f), with a disordered structure. As for aluminium alloy 7075, it can be shown that the behaviour is opposite: increasing the concentration of tartaric acid resulted in an increase in pore diameter (see Table 3) when anodizing process was carried out at 37 °C, with a similar change in porous layer morphology when 55 °C was set as bath temperature. This effect can be probably explained with a stronger oxide dissolution due to the higher bath temperature. In contrast, anodizing at 20 V and 37 °C allowed obtaining smoother surfaces and more ordered porous structures.

The alloy composition has a strong impact on the anodizing process and therefore on the features of the grown anodic layers. Indeed, the intermetallic particles can affect the composition of the barrier layer due the incorporation of species other than Al^{3+} into the anodic layers. This in turn affects the conductivity of the materials and the pores' features. These effects have been described in previous works reported in the literature [47,48]. Moreover, our results are in agreement with what reported in literature: M. Saenz de Miera and coworkers [49] reported that both anodized 2024-T3 and 7075-T6 alloys revealed scalloped surfaces morphology because of peculiar removal of material originated from the differences in reactivity of the intermetallic particles with respect to the aluminium matrix. Same irregular surface after anodizing was detected by M. García-Rubio and co-workers [50] and by Pinheiro and coworkers [51], with a significant lateral porosity, in addition to the typical pore alignment perpendicular to the substrate.

The above reported statements are also supported by the estimate of average pore diameters (Φ_P) displayed in Table 3.

It is worth noting that, especially under certain operating conditions (e.g., anodizing at 55 °C), the pore morphology is not always regular and ordered, which can influence the accuracy of the measurement. The values presented therefore represent mean estimates based on several measurements taken from different micrograph regions, rather than exact pore dimensions. Hence, changing anodizing operating conditions can be considered as a valuable strategy to tailor the anodic oxide morphology of aluminium alloys and, therefore, enhance their corrosion behaviour and interlocking properties.

3.1.2. Corrosion resistance

To evaluate the corrosion resistance of all investigated metallic substrates, and how this parameter is correlated to the oxide morphology resulted, polarization curves and EIS spectra were recorded in a 3.5 wt % NaCl aqueous solution, mimicking seawater, a highly aggressive environment for anodized aluminium alloy [52]. Potentiodynamic polarization curves for anodized 2024-T3 and 7075-T6 samples, are shown in Fig. 4a) and b), respectively.

E_{corr} and E_{pit} values are reported in Table 4.

The current density both in the anodic and cathodic branches is strongly affected by the surface treatment for both aluminium alloys. For AA2024-T3 (see Fig. 4a) the presence of the anodic layer shifts the corrosion potential, E_{corr}, toward more positive values. In fact, E_{corr} is −0.65 V Ag/AgCl in the case of MT sample, as expected since anodic layer increase corrosion resistance of the aluminum alloys. For these samples, it is not possible to clearly locate a passivity region since current density increased before reaching pitting potential, E_{pit}. The latter

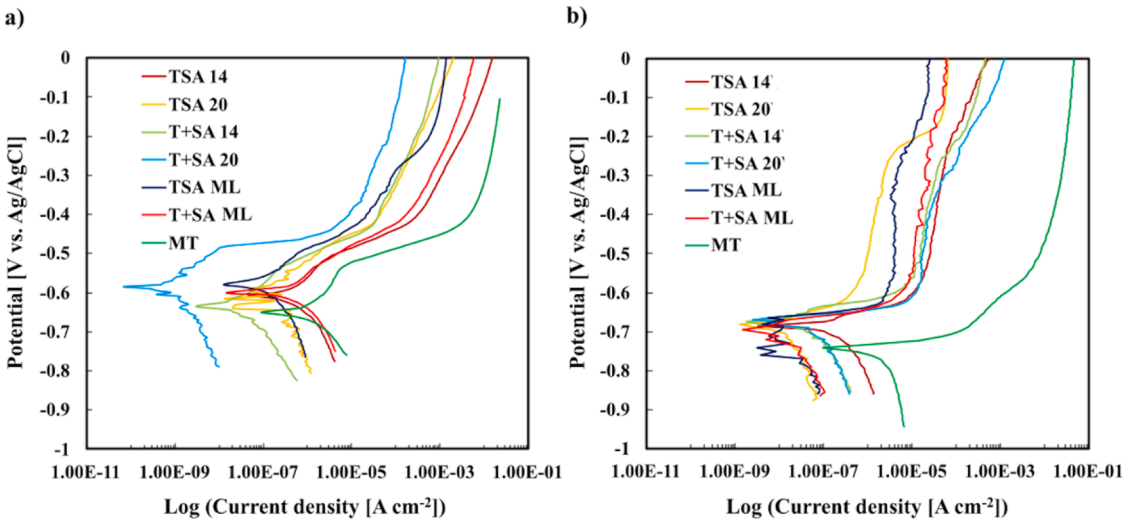

Fig. 4. Potentiodynamic polarization curves recorded in a 3.5 wt % NaCl aqueous solution of a) 2024-T3 and b) 7075-T6 anodized sample.

Table 4
E_{corr} and E_{pit} values estimated from polarization curves shown in Fig. 4.

	2024-T3		7075-T6	
	E_{corr} [V Ag/AgCl]	E_{pit} [V Ag/AgCl]	E_{corr} [V Ag/AgCl]	E_{pit} [V Ag/AgCl]
MT	−0.65 ± 0.05	−0.54 ± 0.07	−0.74 ± 0.07	−0.70 ± 0.06
TSA 14	−0.6 ± 0.03	−0.53 ± 0.02	−0.71 ± 0.03	−0.20 ± 0.03
TSA 20	−0.63 ± 0.03	−0.48 ± 0.02	−0.70 ± 0.04	−0.24 ± 0.05
TSA ML	−0.58 ± 0.02	−0.50 ± 0.02	−0.69 ± 0.02	−0.20 ± 0.02
T+SA 14	−0.64 ± 0.05	−0.53 ± 0.04	−0.70 ± 0.01	−0.25 ± 0.05
T+SA 20	−0.59 ± 0.06	−0.48 ± 0.02	−0.67 ± 0.03	−0.35 ± 0.03
T+SA ML	−0.60 ± 0.05	−0.54 ± 0.02	−0.70 ± 0.02	0.25 ± 0.02

resulted to be slightly more anodic in the case of anodized samples with respect to that related to MT sample, suggesting a lower pitting susceptibility. Notable, in the case of AA sample anodized in T+SA 20 conditions (see Table 2), the entire polarization curve is shifted toward lower current density values, indicating the highest anticorrosion performance, in agreement with its morphology which presents very narrow pores (see Table 3).

In the case of AA 7075-T6 (see Fig. 4b), anodized samples did not show significantly different behaviour, with E_{corr} not changing appreciably by changing anodizing process parameters, being close to −0.7 V Ag/AgCl for all the samples. However, it is evident that MT sample showed the most cathodic E_{corr} and the higher passivity current density, which can be clearly located in polarization curves. This can be related to considerably more anodic E_{pit} values (> −0.35 V Ag/AgCl) with respect to those recorded for 2024-T3 alloys. This can be explained by considering the galvanic coupling effects between intermetallic particles and AA alloy matrix that are stronger in 2024-T3 samples than in 7075-T6 samples due to the peculiar composition of intermetallic particles in AA 2 series (Cu-rich) with respect to those in AA 7 series samples (Zn and Mg-rich).

EIS spectra recorded at the open circuit potential are reported in Nyquist representation in Fig. 5a-b, in 3.5 % NaCl solution, whilst Bode representation of corresponding spectra is reported in Fig. S1 and Fig. S2.

The spectra are depressed semicircles with a diameter resulting to be a function of the anodizing conditions, and were fitted according to the Electrical Equivalent Circuit (EEC) shown in the inset of Fig. 5a, composed by the series of the electrolyte resistance, R_{el}, with a parallel

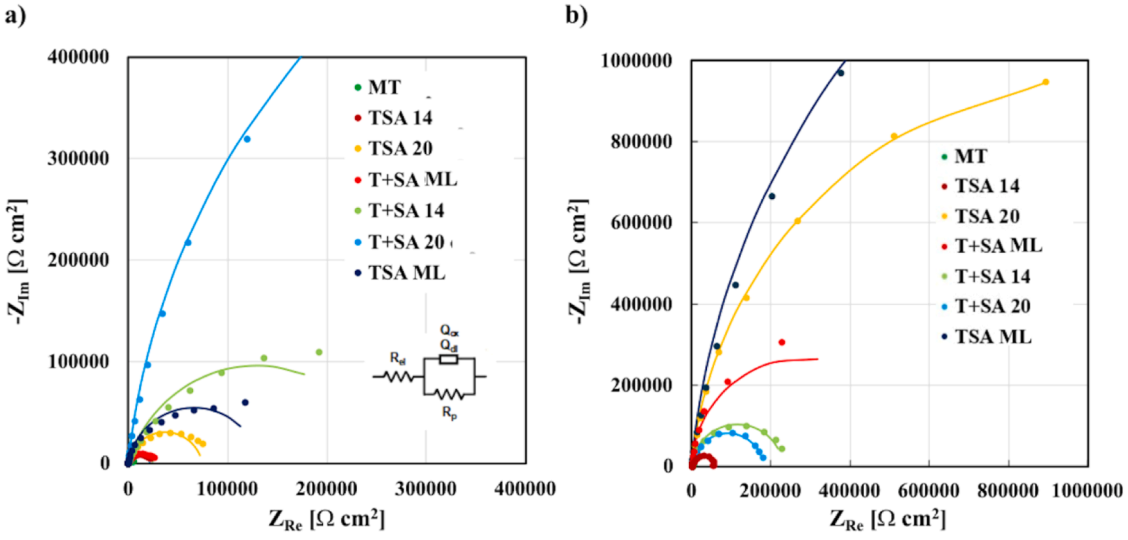

Fig. 5. EIS spectra in Nyquist representation of anodized a) 2024-T3 and b) 7075-T6 samples recorded at corresponding E_{corr} in 3.5 wt % NaCl aqueous solution. Inset: electrical equivalent circuit used for fitting impedance spectra. Fitting: continuous lines.

Table 5
Impedance spectra fitting for all the investigated aluminium alloy samples.

	2024-T3					7075-T6				
	R_{el} [Ω cm^2]	R_p [Ω cm^2]	Q_{dl}, Q_{ox} [S s^n cm^{-2}]	n	d_{ox} [nm]	R_{el} [Ω cm^2]	R_p [Ω cm^2]	Q_{dl}, Q_{ox} [S s^n cm^{-2}]	n	**d_{ox} [nm]**
MT	13	5.7×10^3	5.1×10^{-5}	0.87	–	13	2.6×10^3	1.6×10^{-5}	0.92	–
TSA 14	9	2.2×10^4	5.6×10^{-6}	0.82	12.5	18	5.5×10^4	1.6×10^{-6}	0.92	12
TSA 20	7	7.4×10^4	2.4×10^{-6}	0.88	15	60	2.1×10^6	8.7×10^{-7}	0.93	19
TSA ML	13	1.3×10^5	4.0×10^{-6}	0.88	8	58	3.8×10^6	5.3×10^{-6}	0.94	16
T+SA 14	18	2.5×10^5	3.4×10^{-6}	0.81	14	16	2.3×10^5	1.4×10^{-6}	0.93	13
T+SA 20	11	1.4×10^6	1.0×10^{-6}	0.93	19	20	1.8×10^5	1.2×10^{-6}	0.91	19
T+SA ML	12	2.5×10^4	5.7×10^{-6}	0.85	8	30	5.6×10^5	9.7×10^{-7}	0.97	11

RQ parallel where Q is a constant phase element (CPE), introduced to model the non-ideal interface capacitance. For not anodized alloys, the latter is due to the double layer (Q_{dl}), while for anodized samples this is due to the capacitance of the barrier layer at the bottom of the pores. In both cases CPE is parallel to the polarization resistance. EIS spectra fitting parameters are reported for all the investigated samples (see Table 5).

Among the 2024-T3 samples, the T+SA 20 sample exhibited the highest R_p, which agrees with the findings from the polarization curves (see Fig. 4a). This indicates that the T+SA 20 anodizing process results in the highest corrosion resistance. In the case of 7075-T6 samples, highest R_p was estimated for TSA 20 and TSA ML samples in agreement with the information provided by polarization curves. In both cases, the polarization resistance of best-performing samples is three orders of magnitude higher than that estimated for mechanical polished samples (in fact, the semi-circles of MT in the Nyquist plot are not visible, due to the low R_p), indicating a significant improvement in corrosion resistance. Interesting information is also provided by the values of both modulus of CPE and its exponent n. Indeed, from Q_{ox} values derived from fitting parameter it is possible to estimate the barrier layer capacitance, C_{ox}, using the Brug formula as described in ref [53]. The barrier layer thickness, d_{ox}, can be calculated by knowing C_{ox}, and aluminium oxide dielectric constant, $\varepsilon = 9$, as follows [54]:

$$d_{ox} = \frac{\varepsilon_0 \varepsilon}{C_{ox}} \quad (5)$$

where ε_0 is the vacuum permittivity.

Barrier layer thickness, d_{ox}, as well as the other features of porous anodic layer, such as pore diameter, Φ_P, and the thickness of the oxide layer, d_p (see Fig. 6), can be carefully tailored by controlling the operating parameters of anodizing process. The anodizing time have effect on the d_p, the applied voltage influences d_{ox}, while temperature and composition of the bath affect Φ_P [20].

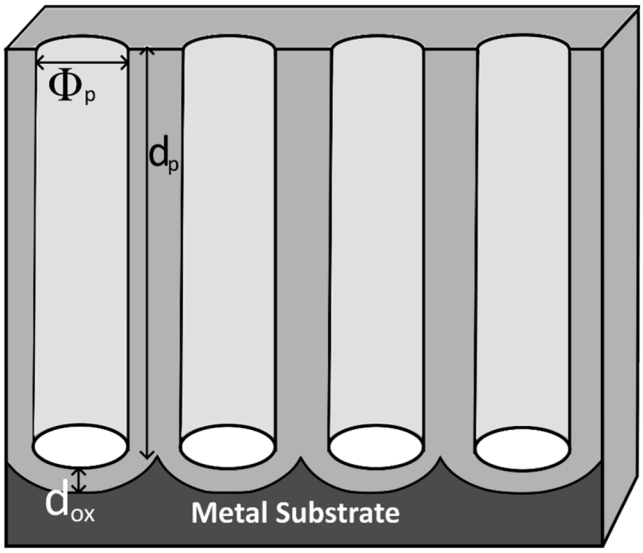

Fig. 6. Sketch of the porous anodic layer grown on aluminium alloys.

For unsealed porous anodic films, a larger d_p makes it more difficult for the aggressive environment to reach the barrier layer, which remains the critical protective element between the substrate and the electrolyte. When the corrosion resistance is evaluated by immersion in seawater-simulating electrolyte, as in this case, d_{ox} value has a stronger impact on corrosion resistance with respect to d_p. For this reason, following discussion focused on the role of the barrier layer thickness and its influence on corrosion protection. For anodized AA2024-T3, d_{ox} is around 8 nm for TSA ML and T+SA ML samples, while the highest value was calculated for T+SA 20 (19 nm), in agreement with the higher formation voltage. The higher barrier layer thickness value, as well as the morphological features of porous layer (i.e. very tiny pores' mouth), hindering the diffusion of chloride ions toward the pores' bottom (see Fig. 2), can explain the high polarization resistance and high pitting potential. Regarding AA7075-T6 alloys, the highest d_{ox} value was estimated for TSA 20 sample (~ 19 nm) and TSA ML (~ 16 nm), i.e. those showing the smallest pore diameter and the highest polarization resistance. Notably, a longer anodizing time induces the formation of longer pores which contributes to make more protective TSA ML alloys.

As explained in the next paragraph, the findings of the electrochemical characterization of anodized samples influenced the selection of the FML samples for mechanical tests.

3.2. Mechanical characterization of FMLs

Among all treatment conditions listed in Table 2, only two anodizing processes were selected for both aluminium alloys studied, to compare them with the mechanically treated samples (MT). This choice was made by selecting anodizing operating parameters that offered both high corrosion resistance and a pore morphology (i.e. pore diameters) would promote optimal adhesion.

Specifically, for FMLs made with 2024-T3 aluminium alloy, TSA 20 was chosen based on preliminary analyses indicating metal substrates with a favourable morphology, (i.e., large pore diameter) despite exhibiting intermediate corrosion resistance (not as low as TSA 14). While T+SA 20 was chosen due to the promising preliminary results in

Table 6
Flexural properties of FMLs at varying anodizing conditions.

Alloys	Codes	Flexural strength [MPa]	Flexural modulus [GPa]	Deformation at break [%]
2024-T3	**MT**	304.8 ± 13.6	46.1 ± 1.0	3.6 ± 0.4
	TSA 20	345.1 ± 8.2	49.3 ± 1.7	4.2 ± 0.3
	T+SA 20	348.6 ± 11.2	48.5 ± 2.7	4.5 ± 0.3
7075-T6	**MT**	289.7 ± 28.4	36.0 ± 6.5	3.8 ± 1.2
	T+SA ML	331.2 ± 11.1	36.6 ± 4.5	4.2 ± 0.2
	TSA 20	323.4 ± 11.9	37.7 ± 4.4	4.3 ± 0.4

terms of best corrosion resistance evidenced by the metal substrate thanks to the presence of small-diameter pores and high barrier layer thickness. On the other hand, the treatments selected for FMLs made with 7075-T6 aluminium alloy were T+SA ML, which allows for suitable pore morphology, i.e., pores with high diameters and intermediate corrosion resistance of the metal substrate, and TSA 20 for high corrosion resistance because of the low pore diameter and high barrier layer thickness.

3.2.1. Three-point bending tests

Three-point bending tests were carried out to evaluate the impact of different anodizing conditions on flexural properties of FMLs.

The experimental results reported in Table 6 clearly evidence that anodizing of the metal substrate consistently improved the mechanical performance of all treated FML samples in comparison to MT ones, regardless of process parameters and aluminium alloy kind (i.e., 2024-T3 and 7075-T6). Indeed, the FMLs made with anodized metallic substrates, have shown improvements in terms of flexural strength, modulus, and deformation at break. Despite the beneficial effect of anodizing on the mechanical response of FMLs in comparison to those made with mechanically treated metal substrates, this test did not reveal any significant differences between the anodizing treatments. This finding is mainly because all the anodized FML samples did not break under three-point bending loads, thanks to their enhanced deformability. Indeed, Fig. 7 clearly shows the example of FML 2024 which, those made with mechanically treated metal substrates, showed adhesive failures between the metal and composite substrates (see inside red box). However, in the case of anodized samples, this specific mechanical test did not cause any failure thanks to their higher metal-to composite interfacial adhesion.

These results are clearer by observing the stress strain curves in Fig. 8. For both FMLs, i.e., with 2024 and 7075 aluminium alloys, the MT samples show a part of the curve after the maximum with a stress drop, signifying local debonding at the interface between metal and composite. These drops are absent in the anodized samples, a sign of the absence of fractures at the interface.

For this reason, three-point bending test results demonstrate that the anodizing techniques selected for their beneficial effect on the metal substrates' morphology and/or corrosion resistance improved the mechanical performance of the FMLs. Nevertheless, further investigation is necessary to understand which anodizing processes result in better stability of FMLs.

3.2.2. Short beam shear tests

Short beam shear tests were conducted to better discriminate the differences in performance of the FML samples with different anodized metallic substrates. Indeed, the interlaminar shear strength of the FMLs was measured through this characterization, which can effectively highlight the actual differences among the effects of all anodizing treatments.

As shown in Fig. 9, the ILSS values of both FMLs, realized with 2024-T3 and 7075-T6 aluminium alloys, exhibited a similar trend. The treatments chosen due to the high porosity obtained on the metal surface, i.e., TSA 20 for 2024-T3 based FMLs and T+SA ML for 7075-T6 based FMLs, respectively, led to the best mechanical performances: +42 % and +46 % compared to their corresponding FMLs made with mechanically treated metal substrates (MT). Reduced increments (+14 % and +21 %) were achieved for 2024-T3 T+SA 20, and 7075-T6 TSA 20 based FMLs in comparison to MT. This different finding can be primarily attributed to the differing surface morphologies of the aluminium alloys resulting from the various anodizing processes. As previously stated, the corrosion resistance is strictly linked to the pore size (i.e., diameter) in the surface layer of the metal substrate. When the obtained pores show small diameter, the corrosion resistance of the metal results high, followed by a decrement in mechanical performance.

As already discussed for the three-point bending tests, even in this case the increment in mechanical performance of the anodized FML samples can be correlated with the different failure modes experienced by FML samples. In more detail, FMLs fabricated with mechanically treated aluminium alloy exhibited a primary adhesive fracture mechanism at the metal-composite interface. On the other hand, the interlaminar failure within the composite observed for all the anodized FMLs (Fig. 10), confirmed the beneficial role played by the anodizing technique on the metal-to-composite interfacial adhesion.

4. Conclusions

This study highlighted the significant impact of anodizing processes, particularly using Tartaric-Sulfuric Acid (TSA) and its modified versions, on the performance of fiber metal laminates (FMLs) made from aluminium alloys (2024-T3 and 7075-T6) and carbon-reinforced polyether ether ketone (PEEK) composites.

Preliminary analyses of aluminium alloys identified two anodizing processes for each metal, among all conditions investigated, that offer both high corrosion resistance and surface morphology conducive to optimal adhesion: TSA 20 and T+SA 20 for AA 2024; T+SA ML and TSA 20 for AA 7075.

The mechanical characterization of the manufactured FMLs showed that the selected anodizing treatments notably enhance the overall mechanical stability of the corresponding FMLs, compared to those made with mechanically treated metal substates (MT).

In particular, the selected anodizing techniques significantly enhanced the maximum flexural strength of anodized FML samples, regardless of the aluminium alloy used as metal substrates. Additionally, short beam shear tests revealed that treatments optimized for high porosity (i.e., TSA 20 for AA2024 and T+SA ML for AA7075) resulted in FMLs with superior interlaminar shear strength values. Conversely, treatments optimized to achieve smaller pores on the metal substates (i.e., T+SA 20 for AA2024 and TSA 20 for AA7075) provide to maintain intermediate interlaminar shear strength values of the related FMLs, increasing at the same time their corrosion resistance of the aluminium alloys

Overall, anodized FMLs consistently outperformed mechanically treated ones, demonstrating that the proposed anodizing process is well-

Fig. 7. Image of FMLs 2024-T3 samples after flexural test.

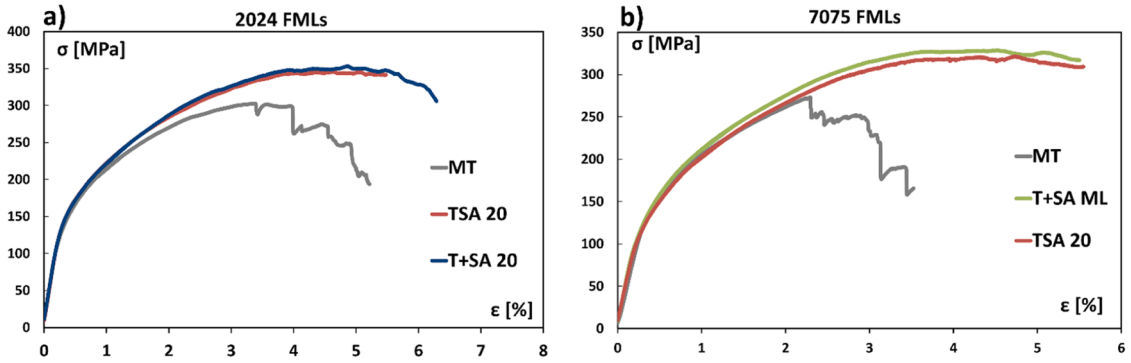

Fig. 8. Stress strain curve varying the surface treatments: a) FMLs 2024, b) FMLs 7075.

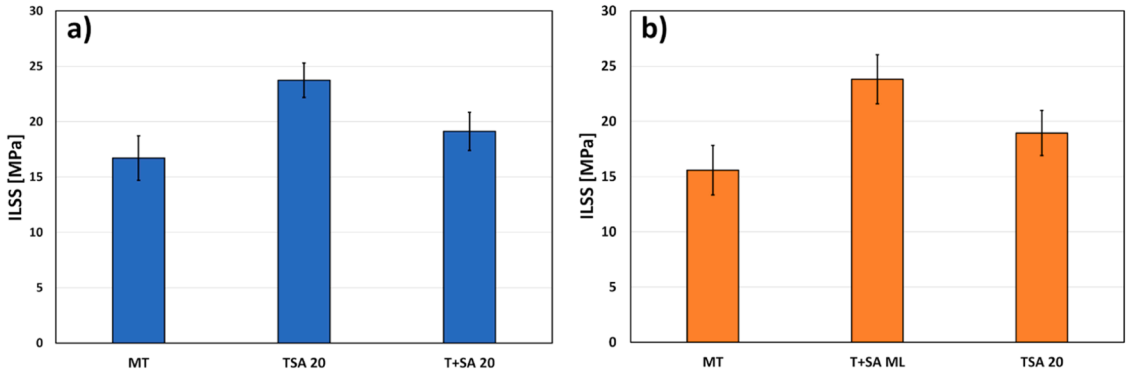

Fig. 9. Interlaminar shear strength average values for a) 2024-T3 FMLs and b) 7075-T6 FMLs.

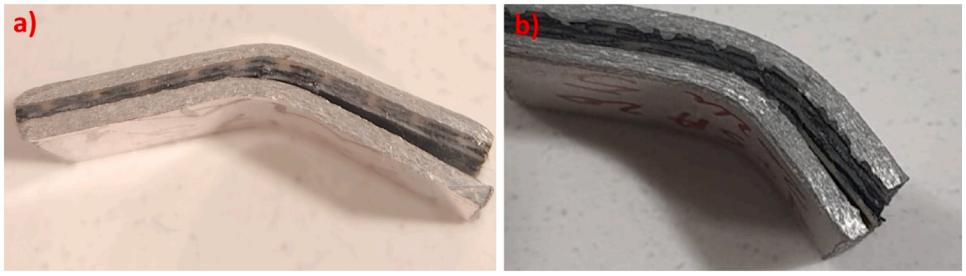

Fig. 10. Example of FML samples after SBS test: a) 2024-T3-MT; b) 2024-T3-TSA 20.

suited for aerospace applications demanding lightweight and robust materials. While anodizing generally enhances mechanical properties, the specific benefits can vary depending on anodizing conditions and aluminium alloy. Therefore, tailored anodizing processes offer a promising approach to improving the durability and structural integrity of FMLs in challenging aerospace environments. However, systematic long-term testing, under thermal cycling or cyclic mechanical loading, or testing more complex scenarios, such as localized corrosion under combined fatigue, stress, and thermal gradients, are needed and they will be carried out in a future paper in order to validate the robustness of oxide-mediated interfaces in practical service conditions.

CRediT authorship contribution statement

R. Miranda: Writing – original draft, Methodology, Investigation, Data curation, Formal analysis, Software, Writing – review & editing. **A. Zaffora:** Writing – original draft, Supervision, Methodology, Data curation, Conceptualization, Formal analysis, Visualization, Writing – review & editing. **V. Fiore:** Writing – review & editing, Supervision, Conceptualization, Visualization. **F. Di Franco:** Writing – review & editing, Supervision, Conceptualization, Visualization. **M. Santamaria:** Writing – review & editing, Supervision, Resources, Conceptualization, Formal analysis, Methodology. **A. Valenza:** Supervision, Resources, Methodology, Writing – review & editing.

Declaration of competing interest

The authors declare that they have no known competing financial interests or personal relationships that could have appeared to influence the work reported in this paper.

Supplementary materials

Supplementary material associated with this article can be found, in the online version, at doi:10.1016/j.surfin.2025.108215.

Data availability

Data will be made available on request.

References

[1] H.M. Karandikar, F. Mistree, Tailoring composite materials through optimal selection of their constituents, J. Mech. Des. 114 (1992) 451–458, https://doi.org/10.1115/1.2926573.

[2] D.D.L. Chung, Structural composite materials tailored for damping, J. Alloys. Compd. 355 (2003) 216–223, https://doi.org/10.1016/S0925-8388(03)00233-0.

[3] A.K. Roy, B.L. Farmer, S. Sihn, V. Varshney, S. Patnaik, S. Ganguli, Thermal interface tailoring in composite materials, Diam. Relat. Mater. 19 (2010) 268–272, https://doi.org/10.1016/j.diamond.2009.10.024.

[4] F. Cavezza, M. Boehm, H. Terryn, T. Hauffman, A review on adhesively bonded aluminium joints in the automotive industry, Met. (Basel) 10 (2020) 1–32, https://doi.org/10.3390/met10060730.

[5] M.D. Banea, M. Rosioara, R.J.C. Carbas, L.F.M. da Silva, Multi-material adhesive joints for automotive industry, Compos. B Eng. 151 (2018) 71–77, https://doi.org/10.1016/j.compositesb.2018.06.009.

[6] G. Jeevi, S.K. Nayak, M.Abdul Kader, Review on adhesive joints and their application in hybrid composite structures, J. Adhes. Sci. Technol. 33 (2019) 1497–1520, https://doi.org/10.1080/01694243.2018.1543528.

[7] S. Budhe, M.D. Banea, S. de Barros, L.F.M. da Silva, An updated review of adhesively bonded joints in composite materials, Int. J. Adhes. Adhes. 72 (2017) 30–42, https://doi.org/10.1016/j.ijadhadh.2016.10.010.

[8] X. Shang, E.A.S. Marques, J.J.M. Machado, R.J.C. Carbas, D. Jiang, L.F.M. da Silva, Review on techniques to improve the strength of adhesive joints with composite adherends, Compos. B Eng. 177 (2019) 107363, https://doi.org/10.1016/j.compositesb.2019.107363.

[9] H. Takahashi, M. Chiba, Role of anodic oxide films in the corrosion of aluminum and its alloys, 36 (2018) 35–54. doi:10.1515/corrrev-2017-0048.

[10] M.P. Martínez-Viademonte, S.T. Abrahami, T. Hack, M. Burchardt, H. Terryn, A review on anodizing of aerospace aluminum alloys for corrosion protection, Coatings 10 (2020) 1–30, https://doi.org/10.3390/coatings10111106.

[11] F. Di Franco, A. Zaffora, M. Santamaria, F. Di Quarto, Anodization and Anodic Oxides, Elsevier Inc., 2018, https://doi.org/10.1016/B978-0-12-409547-2.11704-4.

[12] L. Dong, Y. Li, M. Huang, X. Hu, Z. Qu, Y. Lu, Effect of anodizing surface morphology on the adhesion performance of 6061 aluminum alloy, Int. J. Adhes. Adhes. 113 (2022), https://doi.org/10.1016/j.ijadhadh.2021.103065.

[13] Y. Xu, H. Li, Y. Shen, S. Liu, W. Wang, J. Tao, Improvement of adhesion performance between aluminum alloy sheet and epoxy based on anodizing technique, Int. J. Adhes. Adhes. 70 (2016) 74–80, https://doi.org/10.1016/j.ijadhadh.2016.05.007.

[14] V. Fiore, F. Di Franco, R. Miranda, M. Santamaria, D. Badagliacco, A. Valenza, Effects of anodizing surface treatment on the mechanical strength of aluminum alloy 5083 to fibre reinforced composites adhesive joints, Int. J. Adhes. Adhes. 108 (2021), https://doi.org/10.1016/j.ijadhadh.2021.102868.

[15] M. Mohamad, H.F.A. Marzuki, S.N.A. Bakar, A.N. Abdullah, E.A.E. Ubaidillah, M.F. Z. Abidin, S. Omar, Effect of anodizing electrolyte for structural adhesives bonding study of aluminium-carbon laminates composites, Int. J. Automot. Mech. Eng. 10 (2014) 2091–2101, https://doi.org/10.15282/ijame.10.2014.25.0176.

[16] J.-S. Zhang, X.-H. Zhao, Y. Zuo, J.-P. Xiong, The bonding strength and corrosion resistance of aluminum alloy by anodizing treatment in a phosphoric acid modified boric acid/sulfuric acid bath, Surf. Coat. Technol. 202 (2008) 3149–3156, https://doi.org/10.1016/j.surfcoat.2007.10.041.

[17] F. Di Franco, V. Fiore, R. Miranda, D. Badagliacco, M. Santamaria, A. Valenza, Influence of anodizing surface treatment on the aging behavior in salt-fog environment of aluminum alloy 5083 to fiber reinforced composites adhesive joints, J. Adhes. 99 (2023) 277–296, https://doi.org/10.1080/00218464.2021.2011240.

[18] J. Chen, J. Huang, Y. Wu, K. Du, H. Xiang, Y. Li, C. Yang, X. Xia, Effect of surface anodizing on the bonding properties of aluminum alloy/glass-fiber reinforced polypropylene random copolymer hybrid joints, Int. J. Adhes. Adhes. 123 (2023), https://doi.org/10.1016/j.ijadhadh.2023.103361.

[19] E. Harscoet, D. Froelich, Use of LCA to evaluate the environmental benefits of substituting chromic acid anodizing (CAA), J. Clean. Prod. 16 (2008) 1294–1305, https://doi.org/10.1016/j.jclepro.2007.06.010.

[20] M.P. Martínez-Viademonte, S.T. Abrahami, T. Hack, M. Burchardt, H. Terryn, A review on anodizing of aerospace aluminum alloys for corrosion protection, Coatings 10 (2020) 1–30, https://doi.org/10.3390/coatings10111106.

[21] A. Baldan, Adhesively-bonded joints and repairs in metallic alloys, polymers and composite materials: adhesives, adhesion theories and surface pretreatment, J. Mater. Sci. 39 (2004) 1–49, https://doi.org/10.1023/B:JMSC.0000007726.58758.e4.

[22] G. Di Bella, G. Galtieri, E. Pollicino, C. Borsellino, Mechanical characterization of adhesive joints with dissimilar substrates for marine applications, Int. J. Adhes. Adhes. 41 (2013) 33–40, https://doi.org/10.1016/j.ijadhadh.2012.10.005.

[23] P. Molitor, V. Barron, T. Young, Surface treatment of titanium for adhesive bonding to polymer composites: a review, Int. J. Adhes. Adhes. 21 (2001) 129–136.

[24] S.T. Abrahami, T. Hauffman, J.M.M. De Kok, J.M.C. Mol, H. Terryn, Effect of anodic aluminum oxide chemistry on adhesive bonding of epoxy, J. Phys. Chem. C 120 (2016) 19670–19677, https://doi.org/10.1021/acs.jpcc.6b04957.

[25] A. Asundi, A.Y.N. Choi, Fiber metal laminates: an advanced material for future aircraft, J. Mater. Process. Technol. 63 (1997) 384–394.

[26] T. Sinmazçelik, E. Avcu, M.Ö. Bora, O. Çoban, A review: fibre metal laminates, background, bonding types and applied test methods, Mater. Des. 32 (2011) 3671–3685, https://doi.org/10.1016/j.matdes.2011.03.011.

[27] K. Kavitha, R. Vijayan, T. Sathishkumar, Fibre-metal laminates: a review of reinforcement and formability characteristics, Mater. Today Proc. 22 (2020) 601–605, https://doi.org/10.1016/j.matpr.2019.08.232.

[28] A. Salve, R. Kulkarni, A. Mache, A review: fiber metal laminates (FML's) - manufacturing, test methods and numerical modeling, Int. J. Eng. Technol. Sci. 3 (2016) 71–84, https://doi.org/10.15282/ijets.6.2016.1.10.1060.

[29] H. El Etri, M.E. Korkmaz, M.K. Gupta, M. Gunay, J. Xu, A state-of-the-art review on mechanical characteristics of different fiber metal laminates for aerospace and structural applications, Int. J. Adv. Manuf. Technol. 123 (2022) 2965–2991, https://doi.org/10.1007/s00170-022-10277-1.

[30] P.K. Mallick, Thermoplastics and thermoplastic-matrix composites for lightweight automotive structures, 2010. https://doi.org/10.1016/B978-1-84569-463-0.50004-3.

[31] N.G. Gonzalez-Canche, E.A. Flores-Johnson, P. Cortes, J.G. Carrillo, Evaluation of surface treatments on 5052-H32 aluminum alloy for enhancing the interfacial adhesion of thermoplastic-based fiber metal laminates, Int. J. Adhes. Adhes. 82 (2018) 90–99, https://doi.org/10.1016/j.ijadhadh.2018.01.003.

[32] M. Hou, L. Yee, Y.W. Mai, Manufacturing process and mechanical properties of thermoplastic composite components, J. Mater. Process. Technol. 63 (1997) 334–338, https://doi.org/10.1016/S0924-0136(96)02644-1.

[33] S.A. U, M. Remanan, K. Jayanarayanan, Comparison of properties of carbon Fiber reinforced thermoplastic and thermosetting composites for aerospace applications, Mater. Today Proc. 24 (2020) 453–462. www.sciencedirect.com.

[34] F. Sarasini, J. Tirillò, L. Ferrante, C. Sergi, F. Sbardella, P. Russo, G. Simeoli, D. Mellier, A. Calzolari, Effect of temperature and fiber type on impact behavior of thermoplastic fiber metal laminates, Compos. Struct. 223 (2019) 110961, https://doi.org/10.1016/j.compstruct.2019.110961.

[35] D. Parker, J. Bussink, H.T. van de Grampel, G.W. Wheatley, E.-U. Dorf, E. Ostlinning, K. Reinking, F. Schubert, O. Jünger, R. Wagener, Polymers, high-temperature. Ullmann's Encyclopedia of Industrial Chemistry, Wiley-VCH Verlag GmbH & Co. KGaA, 2012, https://doi.org/10.1002/14356007.a21_449.pub4.

[36] D. Kyriacos, High-temperature engineering Thermoplastics. Brydson's Plastics Materials: Eighth Edition, Elsevier Inc., 2017, pp. 545–615, https://doi.org/10.1016/B978-0-323-35824-8.00021-9.

[37] C. Ji, B. Wang, J. Hu, C. Zhang, Y. Sun, Effect of different preparation methods on mechanical behaviors of carbon fiber-reinforced PEEK-Titanium hybrid laminates, Polym. Test. 85 (2020), https://doi.org/10.1016/j.polymertesting.2020.106462.

[38] S.M. Kurtz, Synthesis and Processing of PEEK For Surgical Implants, 2nd ed., Elsevier Inc., 2019 https://doi.org/10.1016/b978-0-12-812524-3.00002-8.

[39] R.I. Shekar, T.M. Kotresh, P.M.D. Rao, K. Kumar, Properties of high modulus peek yarns for aerospace applications, J. Appl. Polym. Sci. 112 (2009) 2497–2510, https://doi.org/10.1002/app.29765.

[40] S. Verma, N. Sharma, S. Kango, S. Sharma, Developments of PEEK (Polyetheretherketone) as a biomedical material: a focused review, Eur. Polym. J. 147 (2021) 110295, https://doi.org/10.1016/j.eurpolymj.2021.110295.

[41] N. Jiang, H. Lyu, Y. Li, N. Xu, H. Zhang, N. Zhou, X. Zou, D. Zhang, Enhanced interfacial adhesion of CF/PEEK-titanium hybrid laminates via rare-earth coordination interaction, Compos. Sci. Technol. 239 (2023), https://doi.org/10.1016/j.compscitech.2023.110070.

[42] R. Miranda, M. Luciano, V. Fiore, F. Di Franco, M. Santamaria, A. Valenza, Enhanced mechanical performances and corrosion resistance of carbon fibre reinforced PEEK-aluminium alloy fiber metal laminates through an innovative two-step electrochemical treatment, Surf. Interfaces 58 (2025), https://doi.org/10.1016/j.surfin.2025.105831.

[43] M. Curioni, P. Skeldon, E. Koroleva, G.E. Thompson, J. Ferguson, Role of tartaric acid on the anodizing and corrosion behavior of AA 2024 T3 aluminum alloy, J. Electrochem. Soc. 156 (2009) C147–C153, https://doi.org/10.1149/1.3077602.

[44] M.P. Martinez-Viademonte, S.T. Abrahami, M.D. Havigh, K. Marcoen, T. Hack, M. Burchardt, H. Terryn, The role of anodising parameters in the performance of bare and coated aerospace anodic oxide films, Coatings 12 (2022), https://doi.org/10.3390/coatings12070908.

[45] International Standard UNI ISO 14130: Fibre-reinforced plastic composites-Determination of apparent interlaminar shear strength by short-beam method, (1997).

[46] ASTM D790 - Standard Test Methods for Flexural Properties of Unreinforced and Reinforced Plastics, 2003.

[47] M. Saenz de Miera, M. Curioni, P. Skeldon, G.E. Thompson, The behaviour of second phase particles during anodizing of aluminium alloys, Corros. Sci. 52 (2010) 2489–2497, https://doi.org/10.1016/j.corsci.2010.03.029.

[48] Y. Ma, X. Zhou, G.E. Thompson, M. Curioni, X. Zhong, E. Koroleva, P. Skeldon, P. Thomson, M. Fowles, Discontinuities in the porous anodic film formed on AA2099-T8 aluminium alloy, Corros. Sci. 53 (2011) 4141–4151, https://doi.org/10.1016/j.corsci.2011.08.023.

[49] M. Saenz De Miera, M. Curioni, P. Skeldon, G.E. Thompson, Preferential anodic oxidation of second-phase constituents during anodising of AA2024-T3 and AA7075-T6 alloys, Surf. Interface Anal. 42 (2010) 241–246, https://doi.org/10.1002/SIA.3191.

[50] M. García-Rubio, M.P. de Lara, P. Ocón, S. Diekhoff, M. Beneke, A. Lavía, I. García, Effect of postreatment on the corrosion behaviour of tartaric–sulphuric anodic films, Electrochim. Acta 54 (2009) 4789–4800, https://doi.org/10.1016/J.ELECTACTA.2009.03.083.

[51] J.S. Pinheiro, C.T. Oliveira, G. Regio, N. Goi, J.Z. Ferreira, J.S. Pinheiro, C. T. Oliveira, G. Regio, N. Goi, J.Z. Ferreira, Characterization of anodized and bare 7075-T6 aluminum alloy treated with Zr-based conversion coating, Tecnol Met. Mater Min 18 (2021), https://doi.org/10.4322/2176-1523.20202407, 0–0.

[52] B.J. Usman, F. Scenini, M. Curioni, The effect of exposure conditions on performance evaluation of post-treated anodic oxides on an aerospace aluminium alloy: comparison between salt spray and immersion testing, Surf. Coat. Technol. 399 (2020) 126157, https://doi.org/10.1016/J.SURFCOAT.2020.126157.
[53] B. Hirschorn, M.E. Orazem, B. Tribollet, V. Vivier, I. Frateur, M. Musiani, Determination of effective capacitance and film thickness from constant-phase-element parameters, Electrochim. Acta 55 (2010) 6218–6227, https://doi.org/10.1016/j.electacta.2009.10.065.
[54] A. Zaffora, F. Di Franco, M. Santamaria, H. Habazaki, F. Di Quarto, The influence of composition on band gap and dielectric constant of anodic Al-Ta mixed oxides, Electrochim. Acta 180 (2015) 666–678, https://doi.org/10.1016/j.electacta.2015.08.068.